



Trans. Nonferrous Met. Soc. China 33(2023) 2784-2798

Transactions of Nonferrous Metals Society of China

www.tnmsc.cn



Experimental determination and thermodynamic calculation of phase equilibria in Ag–Zr–Y system

Cheng-gang JIN^{1,2}, Biao HU^{1,2}, Yu-chao SHI^{1,2}, Shao-ding SHENG ^{1,2}, Shu-hong LIU³, Yong DU³, Jie-qiong HU⁴

1. School of Materials Science and Engineering,

Anhui University of Science and Technology, Huainan 232001, China;

- 2. Anhui International Joint Research Center for Nano Carbon-based Materials and Environmental Health, Anhui University of Science and Technology, Huainan 232001, China;
 - 3. State Key Laboratory of Powder Metallurgy, Central South University, Changsha 410083, China;
 - 4. Sino-Precious Metals Holding Co., Ltd., Kunming 650000, China

Received 20 March 2022; accepted 10 June 2022

Abstract: The phase equilibria of the Ag–Zr–Y system at 800, 600 and 500 °C were investigated by means of X-ray diffraction (XRD) and scanning electron microscope (SEM) with energy dispersive X-ray spectrometry (EDS) techniques. The solubilities of Y in the Ag₂Zr and AgZr phases and of Zr in the Ag₅₁Y₁₄, Ag₂Y and AgY phases were measured, and no ternary compound was found in these isothermal sections. By means of the CALPHAD method, thermodynamic parameters of the Ag–Zr–Y system were assessed based on the experimental data from the present work and the literature. Substitutional solution model was used to describe the solution phases and sublattice models were used to describe binary compounds. A set of self-consistent and accurately described thermodynamic parameters of the Ag–Zr–Y system were obtained. The representative isothermal sections and liquidus projection were calculated, and the Hill reaction scheme of the Ag–Zr–Y system was constructed. The calculated results are in agreement with the experimental data.

Key words: Ag-Zr-Y ternary system; phase equilibria; experimental determination; thermodynamic modeling; CALPHAD method

1 Introduction

Ag-based alloys were widely used in biomaterials [1], photocatalytic materials [2,3] and coating materials [4] due to their advantages of unique chemical, physical, electronic and optical properties. In Ag-based alloys, the addition of rare-earth can refine grain, improve mechanical properties and thermal stability of matrix metals, and improve recrystallization temperature [5,6]. Y is a rare-earth, and the Y-added alloys were widely studied. The addition of Y has different roles in

different alloys likewise enhancing the strength properties of alloys [7–9], improving the structure of alloys [10], and inhibiting interfacial void formation of matrix materials [11]. For sterling Ag, increasing the Y content can improve the corrosion resistance [12]. Adding a small amount of Zr is a useful way to decrease the diffusion rate of Ag for promoting a homogeneous and slower continuous decomposition reaction [13]. Accurate phase constitution and thermodynamic parameters are the key to the design and manufacture of Ag-based advanced materials. The phase diagram of the Ag–Zr–Y system is very crucial for the deep study

of Ag-based alloys.

However, the experimental phase equilibria data of the Ag-Zr-Y system reported in the literature are limited. Only HE et al [14] studied the phase equilibrium relationships of the Ag-Zr-Y system and determined six three-phase regions in the Ag-Zr-Y system at 750 °C. The solubilities of the third elements in binary phases were measured and no ternary compound was found. However, only one isothermal section was experimentally determined and no thermodynamic description of the Ag-Zr-Y system was reported in Ref. [14]. It is hard to obtain a set of accurate thermodynamic parameters of the ternary system based on the limited experimental data. Considering the practical applications in heat treatment, the experimental temperatures should be higher than recovery temperature of the phases in the Ag-Zr-Y system. In addition, based on the phase diagrams of the binary systems, the lowest stable existence temperature of liquid phase in the Ag-Y system is about 800 °C. For those reasons, the purposes of the present work are to experimentally determine the phase equilibria of the Ag-Zr-Y system at 800, 600 and 500 °C by means of X-ray diffraction (XRD) and scanning electron microscopy (SEM) with energy dispersive X-ray spectrometry (EDS) and to thermodynamically assess this system by the CALPHAD method [15–17].

2 Literature review

To facilitate reading, the equilibrium phases and their crystal structures in the Ag-Zr-Y system are listed in Table 1.

2.1 Ag-Zr binary system

The Ag-Zr binary system has only two intermetallic compounds, i.e., AgZr and AgZr₂. The first complete phase diagram of the Ag-Zr system was constructed by ZHANG et al [20]. The enthalpies of formation of the AgZr and AgZr₂ phases at 25 °C were determined by FITZNER and KLEPPA [21]. The thermodynamic parameters of the Ag-Zr system were assessed by several researchers [18,22-24], in which the thermodynamic parameters from HSIAO et al [18] well reproduced experimental phase diagram data and enthalpies of formation for compounds and were adopted in the present work. The calculated Ag-Zr phase diagram was shown in Fig. 1(a) according to the thermodynamic parameters from HSIAO et al [18].

2.2 Ag-Y binary system

The Ag-Y binary system contains three intermetallic compounds, i.e., AgY, Ag2Y and Ag₅₁Y₁₄. MCMASTERS et al [25] reported the stoichiometry of the Ag₅₁Y₁₄ phase. The phase diagram of the Ag-Y system was reported by GSCHNEIDNER and CALDERWOOD [19]. Then, the Ag-Y system was thermodynamically assessed using the sublattice model and Thermo-Calc software by WANG et al [26], and using the Compound Energy Formalism (CEF) model and FactSage software by WANG et al [27], respectively. WANG et al [27] used the CEF model to describe AgY considering its natural ordered bcc B2 part from disordered bcc A2 solution and to describe Ag₅₁Y₁₄ with a small homogeneity range. However, the calculated results are not in

Table 1 Equilibrium phases and their crystal structures in Ag-Zr-Y system

Phase	Prototype	Personal symbol	Space group	Phase description	Ref.
(Ag)	Cu	cF4	Fm3m	Solid solution based on fcc_A1 Ag	[18]
$(\beta Zr, \beta Y)$	W	cI2	$Im\overline{3}m$	Solid solution based on bcc_A2 Zr and Y	[18,19]
$(\alpha Zr, \alpha Y)$	Mg	hP2	P63/mmc	Solid solution based on hcp_A3 Zr and Y	[18,19]
AgZr	γ-CuTi	tP4	P4/nmm	Binary phase AgZr	[18]
Ag_2Zr	$MoSi_2$	<i>tI</i> 6	I4/mmm	Binary phase Ag ₂ Zr	[18]
AgY	CsCl	cP2	$Pm\overline{3}m$	Binary phase AgY	[19]
Ag_2Y	$MoSi_2$	<i>tI</i> 6	I4/mmm	Binary phase Ag ₂ Y	[19]
$Ag_{51}Y_{14}$	$Ag_{51}Gd_{14} \\$	hP65	P/6m	Binary phase Ag ₅₁ Y ₁₄	[19]

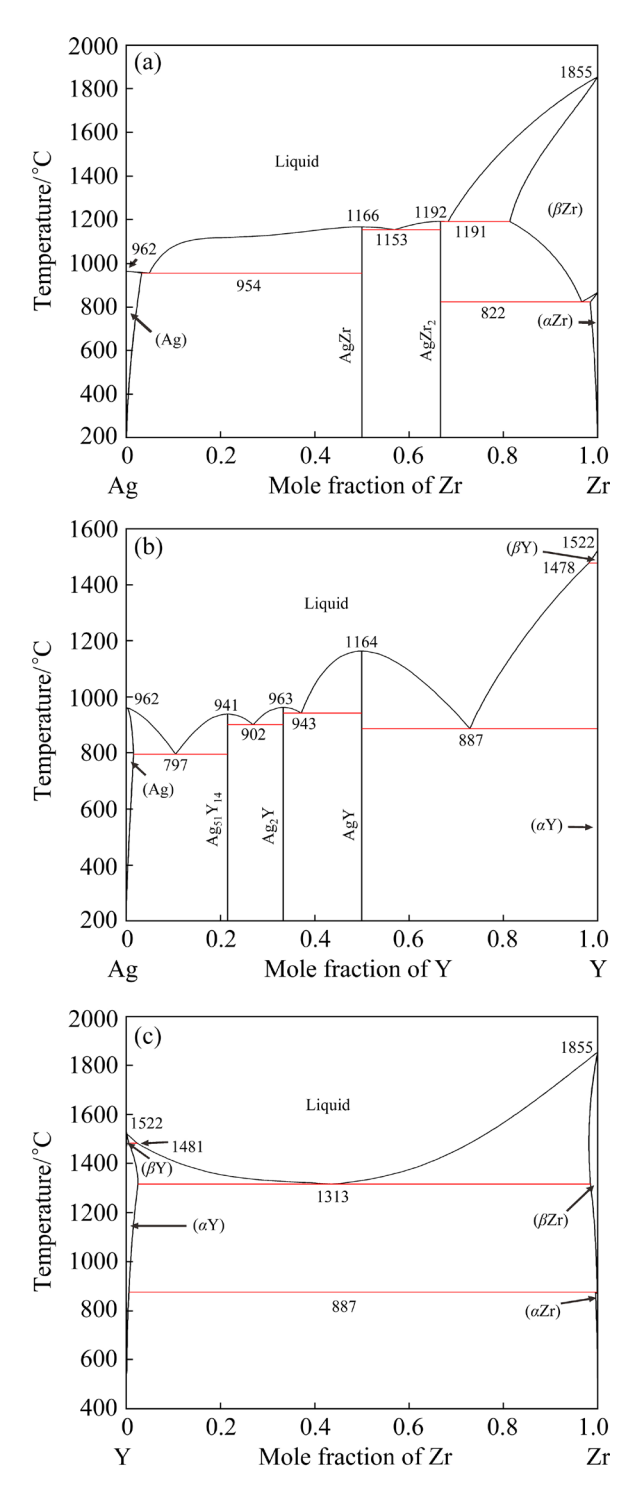


Fig. 1 Calculated phase diagrams of Ag–Zr (a), Ag–Y (b) and Zr–Y (c) using thermodynamic parameters from HSIAO et al [18], WANG et al [26] and BU et al [29], respectively

agreement with part of experimental data using the CEF model. Considering the compatibility in ternary system, the sublattice model was better than CEF model to describe the Ag-Y system in the present work. Therefore, the thermodynamic

parameters from WANG et al [26] were adopted in the present work and the calculated Ag-Y phase diagram was shown in Fig. 1(b).

2.3 Zr-Y binary system

The phase equilibria of the Zr–Y binary system are simple because they only contain solution phases, i.e., liquid, (αZr) , (βZr) , (αY) and (βY) . The phase diagram of the Zr–Y system was first assessed by PALENZONA and CIRAFICI [28]. However, the transformation type and temperature between (αY) and (βY) in the Zr–Y system are controversial in the literature. Recently, BU et al [29] have experimentally studied these issues and reassessed the Zr–Y system. The calculated Zr–Y phase diagram was shown in Fig. 1(c) according to the thermodynamic parameters from BU et al [29].

2.4 Ag-Zr-Y ternary system

The phase equilibria data of the Ag-Zr-Y system are very limited. Only one piece of experimental data was reported by HE et al [14]. The isothermal section at 750 °C was investigated experimentally by the diffusion-triple technology, SEM and electron probe microanalysis. Six threephase regions, i.e., $(\alpha Y) + (\alpha Zr) + AgY$, $Ag_2Y +$ $AgY + (\alpha Zr), Ag_2Y + Ag_{51}Y_{14} + AgZr_2, Ag_2Y +$ $AgZr_2 + (\alpha Zr)$, $Ag_{51}Y_{14} + AgZr + AgZr_2$ and $Ag_{51}Y_{14} + AgZr + (Ag)$, were determined. No ternary compound was found. The measured solubilities of Zr in AgY and Ag51Y14 and Y in AgZr₂ are approximately 1.5, 2.2 and 1.5 at.%, respectively. The solubilities of Zr in Ag₂Y and Y in AgZr are very small and can be negligible. The experimental data reported by HE et al [14] were used in the present work for comparison, analysis and assessment.

3 Experimental

Isothermal sections of the Ag–Zr–Y system at 800, 600 and 500 °C were experimentally determined. Silver rods, zirconium rods and yttrium pieces with a purity of 99.99% (China New Metal Materials Technology Co., Ltd.) were used as raw materials. The nominal compositions of the samples were listed in Table 2 in detail. Twelve ternary alloys, each with a mass of approximately 1 g, were

Table 2 Phases and compositions of Ag–Zr–Y alloys annealed at 800, 600 and 500 $^{\circ}$ C determined by XRD and SEM–EDS at 25 $^{\circ}$ C

Alloy	Nominal composition/at.%	Annealed time/d	Temperature/ °C	Phaseidentified	Composition/at.%			
No.					Ag	Zr	Y	
1				(aZr)	0.90 ± 0.01	97.08±0.06	2.02±0.01	
	$Ag_{20}Zr_{20}Y_{60}$	40	800	(αY)	0.01 ± 0.01	3.53 ± 0.02	96.47 ± 0.07	
				AgY	49.45±0.36	1.60 ± 0.02	48.95 ± 0.32	
				(aZr)	1.94±0.02	98.06±0.96	0.02±0.02	
2	$Ag_{47}Zr_{20}Y_{33} \\$	40	800	Ag_2Y	65.12 ± 0.78	$3.23{\pm}0.07$	31.65 ± 0.02	
				AgY	50.86 ± 0.97	2.84 ± 0.01	46.30 ± 0.02	
				(aZr)	2.30±0.02	97.70±0.04	0.02±0.02	
3	$Ag_{47}Zr_{33}Y_{20} \\$	40	800	$AgZr_2$	33.60±0.11	65.82 ± 0.24	0.58 ± 0.01	
				Ag_2Y	68.57±0.31	1.72 ± 0.02	29.71±0.22	
4				AgZr ₂	35.64±0.14	63.17±0.01	1.19±0.12	
	$Ag_{63}Zr_{17}Y_{20}$	40	800	$Ag_{51}Y_{14}$	76.96±0.18	2.10 ± 0.10	20.94±0.22	
				Ag_2Y	67.22±1.22	2.10±0.01	30.68 ± 0.32	
	$Ag_{73}Zr_{20}Y_{7}$	50	600	(Ag)	97.11±1.55	1.00±0.04	1.89±0.03	
5				AgZr	52.09±1.08	46.79±0.48	1.12±0.01	
				$Ag_{51}Y_{14}$	77.49±0.63	2.40 ± 0.04	20.11 ± 0.38	
6	$Ag_{47}Zr_{20}Y_{33}$	50	600	(aZr)	1.69±0.04	97.84±0.33	0.47±0.01	
				Ag_2Y	65.64 ± 0.63	1.72 ± 0.02	32.46 ± 0.43	
				AgY	49.59±1.02	3.38 ± 0.02	47.03 ± 0.56	
	$Ag_{54}Zr_{40}Y_6$	50	600	Ag ₅₁ Y ₁₄	77.89±0.51	1.12±0.02	20.99±0.05	
7				$AgZr_2$	37.46±0.50	61.69±0.41	0.58 ± 0.01	
				AgZr	48.91±0.71	49.71±0.56	1.38 ± 0.01	
8	$Ag_{43}Zr_{40}Y_{17}$	50	600	(aZr)	7.40±0.03	92.6±0.65	0.01±0.01	
				$AgZr_2$	33.50±0.30	66.09 ± 0.08	0.41 ± 0.22	
				Ag_2Y	66.04±0.51	2.08 ± 0.01	31.88 ± 0.34	
9				(aZr)	0.40±0.01	96.77±0.57	2.83±0.02	
	$Ag_{14}Zr_{40}Y_{46} \\$	50	600	(αY)	3.13 ± 0.11	9.73 ± 0.21	88.14±0.51	
				AgY	47.63±0.53	2.44 ± 0.05	49.93 ± 0.02	
10				(Ag)	94.82±1.01	0.69±0.01	4.49±0.03	
	$Ag_{80}Zr_{10}Y_{10} \\$	60	500	AgZr	50.65±1.34	48.62 ± 0.43	0.73 ± 0.01	
				$Ag_{51}Y_{14}$	79.55±1.31	0.78 ± 0.01	19.67±0.21	
11				(aZr)	3.22±0.02	95.89±1.08	0.89±0.01	
	$Ag_{52}Zr_{10}Y_{38} \\$	60	500	Ag_2Y	66.23±1.07	1.02 ± 0.01	32.75 ± 0.05	
				AgY	49.93±1.13	2.35±0.01	47.72±1.11	
				Ag ₅₁ Y ₁₄	77.92±0.85	1.12±0.31	20.96±0.35	
12	$Ag_{60}Zr_{30}Y_{10} \\$	60	500	$AgZr_2$	35.73±0.71	64.27 ± 0.92	0.02 ± 0.01	
				AgZr	48.91±1.22	49.71±0.85	1.38±0.01	

prepared in a non-consumable vacuum arc-melting furnace (WK-I, Physcience Opto-electronics Co., Ltd., Beijing, China) with a water-cooled copper crucible under a 99.999% pure Ar atmosphere. To improve their homogeneities, each alloy was re-melted at least 4 times. Since the mass losses were less than 2 wt.% for all alloys, the alloys after arc melting were not subjected to chemical analysis. With a vacuum sealing machine (MRVS-1002, Wuhan Bailibo Technology Co., Ltd., China), the button samples were sealed in evacuated quartz capsules and put in a high-temperature diffusion furnace (KSL-1200X, Hefei Kejing Material Technology Co., Ltd., China) and annealed at 800 °C (40 d), 600 °C (50 d) and 500 °C (60 d), followed by quenching in cold water.

After standard metallographic preparation, Cu K_{α} radiation at 40 kV, 300 mA (Smartlab SE, Rigaku Corporation, Japan) and 25 °C was used to test the annealed alloys. Diffraction patterns were generally acquired at a scan step of 0.02° in a 2θ range of $20^{\circ}-80^{\circ}$. After that, the samples were further examined using SEM equipped with EDS (acceleration voltage 20 kV, and working distance 4.5 mm) (JSM-6360LV/GENESIS2000XM60, JEOL, Japan). In addition, three points of each phase were measured by EDS analysis, and the average value was taken as the phase composition.

4 Thermodynamic model

The Gibbs energy functions of the pure elements Ag, Zr and Y were taken from the Scientific Group Thermodata Europe (SGTE) database compiled by DINSDALE [30]. The thermodynamic parameters for the Ag–Zr, Ag–Y and Zr–Y systems from HSIAO et al [18], WANG et al [26] and BU et al [29] were adopted in the present work, respectively. The calculated binary phase diagrams were presented in Fig. 1.

4.1 Solution phases

The solution phases, i.e., liquid, (αZr) , (βZr) , (αY) , (βY) and (Ag), were described by the substitutional solution model [31,32] with the Redlich-Kister-Muggianu polynomial [33]. For example, the molar Gibbs energy of the (Ag) phase is expressed as follows:

$$G^{(Ag)} = x_{Ag}^{o} G_{Ag}^{(Ag)} + x_{Zr}^{o} G_{Zr}^{(Ag)} + x_{Y}^{o} G_{Y}^{(Ag)} +$$

$$RT(x_{Ag} \ln x_{Ag} + x_{Zr} \ln x_{Zr} + x_{Y} \ln x_{Y}) +$$

$$x_{Ag} x_{Zr} L_{Ag,Zr}^{(Ag)} + x_{Ag} x_{Y} L_{Ag,Y}^{(Ag)} +$$

$$x_{Zr} x_{Y} L_{Zr,Y}^{(Ag)} + x_{Ag} x_{Zr} x_{Y} (x_{Ag}^{0} L_{Ag,Zr,Y}^{(Ag)} +$$

$$x_{Zr}^{1} L_{Ag,Zr,Y}^{(Ag)} + x_{Y}^{2} L_{Ag,Zr,Y}^{(Ag)})$$

$$(1)$$

where R represents the molar gas constant, T represents the thermodynamic temperature, and x_{Ag} , x_{Zr} and x_{Y} are the molar fractions of the elements Ag, Zr and Y, respectively. ${}^{0}L_{Ag,Zr,Y}^{(Ag)}$, ${}^{1}L_{Ag,Zr,Y}^{(Ag)}$ and ${}^{2}L_{Ag,Zr,Y}^{(Ag)}$ are ternary interaction parameters that are linearly temperature-dependent and can be expressed as $L_{Ag,Zr,Y}^{(Ag)} = A + BT$. The coefficients A and B will be optimized according to the experimental data available in the present work and the literature.

4.2 Binary phases extending into ternary system

According to the experimental data from HE et al [14] and the present work, the binary phases $Ag_{51}Y_{14}$, $Ag_{2}Y$ and AgY in the Ag-Y system exhibit extended solubilities of Zr, and the binary phases AgZr and $AgZr_{2}$ in the Ag-Zr system exhibit extended solubilities of Y. Sublattice models [34,35] were used to describe these binary phases as $(Ag)_{m}(Y,Zr)_{n}$. In view of the experimental results, it was assumed that Zr and Y substitute each other in the sublattice models. In accordance with the formula for the sublattice model, taking $Ag_{51}Y_{14}$ as an example, the Gibbs energy can be expressed as follows:

$$G^{Ag_{51}Y_{14}} = y_{Y}'' {}^{o}G_{Ag;Y}^{Ag_{51}Y_{14}} + y_{Zr}'' {}^{o}G_{Ag;Zr}^{Ag_{51}Y_{14}} +$$

$$14RT(y_{Y}'' \ln y_{Y}'' + y_{Zr}'' \ln y_{Zr}'') + y_{Y}'' y_{Zr}'' \cdot$$

$$[{}^{0}L_{Ag;Y,Zr}^{Ag_{51}Y_{14}} + (y_{Y}'' - y_{Zr}''){}^{1}L_{Ag;Y,Zr}^{Ag_{51}Y_{14}} + \cdots]$$
(2)

where $y_{\rm Y}''$ and $y_{\rm Zr}''$ are the site fractions of Y and Zr in the second sublattice, respectively. The parameters ${}^{\rm o}G_{{\rm Ag:Y}}^{{\rm Ag_{51}}{\rm Y}_{14}}$ and ${}^{\rm o}G_{{\rm Ag:Zr}}^{{\rm Ag_{51}}{\rm Y}_{14}}$ correspond to the Gibbs energies of the end-members ${\rm Ag_{51}}{\rm Y}_{14}$ and ${\rm Ag_{51}}{\rm Zr}_{14}$, respectively. The interaction parameters ${}^{\rm o}L_{{\rm Ag:Y,Zr}}^{{\rm Ag_{51}}{\rm Y}_{14}}$ and ${}^{\rm l}L_{{\rm Ag:Y,Zr}}^{{\rm Ag_{51}}{\rm Y}_{14}}$ are also linearly temperature-dependent, which can be expressed as $L_{{\rm Ag:Y,Zr}}^{{\rm Ag_{51}}{\rm Y}_{14}} = a+bT$, and the coefficients a and b will be optimized according to the experimental data. Analogous expressions similar to Eq. (2) were used to describe

the Gibbs energies of the Ag_2Y , AgY, $AgZr_2$ and AgZr phases.

5 Results and discussion

5.1 Experimental results and discussion

Twelve alloys were prepared to determine the phase equilibria of the Ag–Zr–Y system at 800, 600 and 500 °C. The phases were identified by XRD, and the composition and microstructure were measured by SEM–EDS. The phases of alloys can be distinguished based on the contrast of microstructure images and composition. The experimental results are listed in Table 2 in detail. No ternary compound was found in these isothermal sections at 800, 600 and 500 °C.

Alloys 1–4 were prepared for determining the isothermal sections of the Ag–Zr–Y system annealed at $800\,^{\circ}$ C. Figure 2 shows the backscattered electron (BSE) micrographs and XRD patterns of Alloys 1 and 4 annealed at $800\,^{\circ}$ C for 40 d. According to the SEM–EDS and XRD results, Alloy 1 (Ag₂₀Zr₂₀Y₆₀) is located in the three-phase region, i.e., dark (α Y) + dark gray AgY + light gray (α Zr), as shown in Figs. 2(a) and (b). Figure 2(c)

shows BSE micrograph for (Ag₆₃Zr₁₇Y₂₀) which is located in the three-phase region. Figure 2(d) shows the XRD pattern for Alloy 4, where the characteristic diffraction peaks of AgZr₂ and Ag₂Y are present but those of Ag₅₁Y₁₄ are in low intensity and pretty hard distinguished. With different additions of Ag, different phases show different contrasts and the Ag51Y14 phase is easily distinguished in BSE micrographs. Combined with the results of BSE micrographs and EDS composition analysis, the Ag₅₁Y₁₄ was identified and Alloy 4 was determined to be located in $Ag_{51}Y_{14} + AgZr_2 + Ag_2Y$. Likewise, the phases of Alloys 2 (Ag₄₇Zr₂₀Y₃₃) and 3 (Ag₄₇Zr₃₃Y₂₀) were also determined, and their XRD patterns were shown in Figs. 3(a) and (b). According to the XRD results and EDS composition analysis, Alloys 2 and 3 were located in three-phase region, i.e., (αZr) + $Ag_2Y + AgY$ and $(\alpha Zr) + AgZr_2 + Ag_2Y$, respectively. Based on the experimental analysis above, the phase equilibria of the Ag-Zr-Y system at 800 °C were obtained in the present work and four three-phase regions were determined: AgZr₂ + $Ag_{51}Y_{14} + Ag_{2}Y$, $(\alpha Zr) + AgZr_{2} + Ag_{2}Y$, $(\alpha Zr) +$ $Ag_2Y + AgY$ and $(\alpha Zr) + (\alpha Y) + AgY$. According to

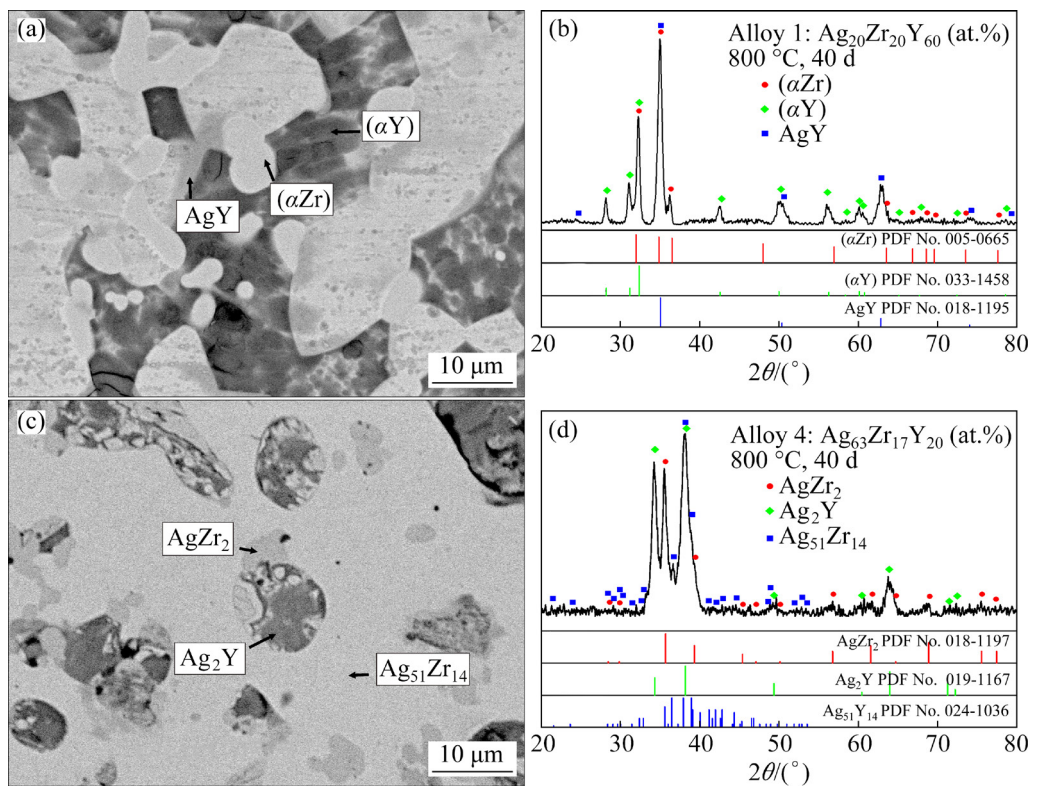


Fig. 2 BSE images (a, c) and XRD patterns (b, d) of Ag–Zr–Y alloys annealed at 800 °C for 40 d: (a, b) Alloy 1 $(Ag_{20}Zr_{20}Y_{60})$; (c, d) Alloy 4 $(Ag_{63}Zr_{17}Y_{20})$

the phase regions of the isothermal section at 750 °C from HE et al [14] and the Gibbs phase rule, two three-phase regions $(Ag) + AgZr + Ag_{51}Y_{14}$ and $AgZr + AgZr_2 + Ag_{51}Y_{14}$ were extrapolated. According to the eutectic reaction: liquid = $Ag_{51}Y_{14} + (Ag)$ at 797 °C in the Ag-Y system [26], the liquid phase exists in the isothermal section at 800 °C in the Ag-Zr-Y system. Combined with Gibbs phase rule [36], a three-phase region of liquid + $(Ag) + Ag_{51}Y_{14}$ was extrapolated. The measured solubilities of Ag and Zr in (αY) , of Zr in

 $Ag_{51}Y_{14}$, Ag_2Y and AgY and of Y in $AgZr_2$ at 800 °C are approximately 0.01, 3.53, 2.10, 2.35, 2.22 and 0.89 at.%, respectively.

Five alloys (Alloys 5–9) were used to determine the isothermal section of the Ag–Zr–Y system at 600 °C by SEM–EDS and XRD analysis. Figure 4 shows the BSE micrographs and XRD patterns of Alloys 5 and 8 annealed at 600 °C for 50 d. In Fig. 4(a), the BSE micrograph of Alloy 5 (Ag₇₃Zr₂₀Y₇) has three-phase region. The characteristic diffraction peaks of Ag₅₁Y₁₄ are also

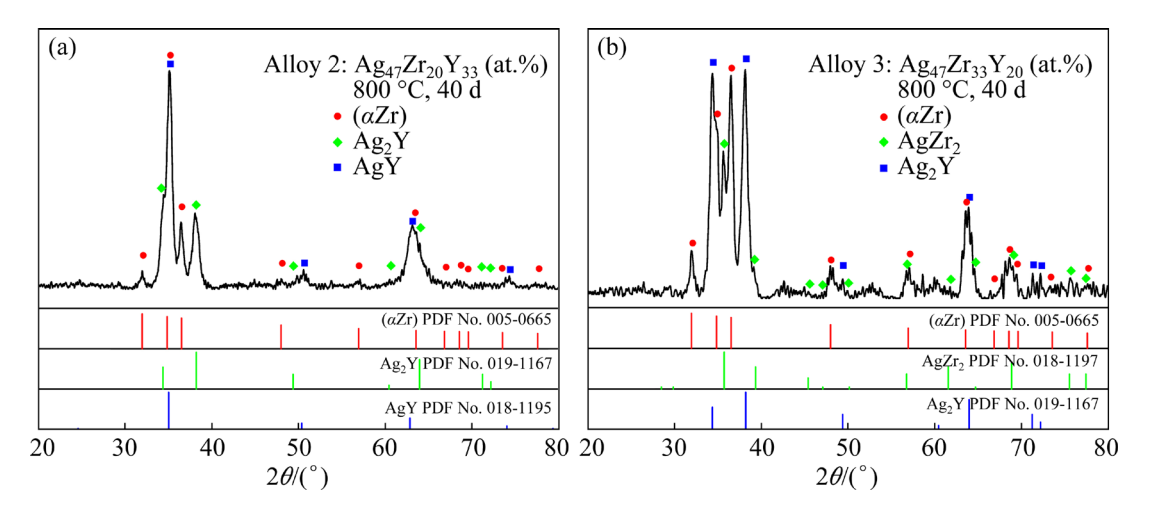


Fig. 3 XRD patterns of Alloy 2 (Ag₄₇Zr₂₀Y₃₃) (a) and Alloy 3 (Ag₄₇Zr₃₃Y₂₀) (b) annealed at 800 °C for 40 d

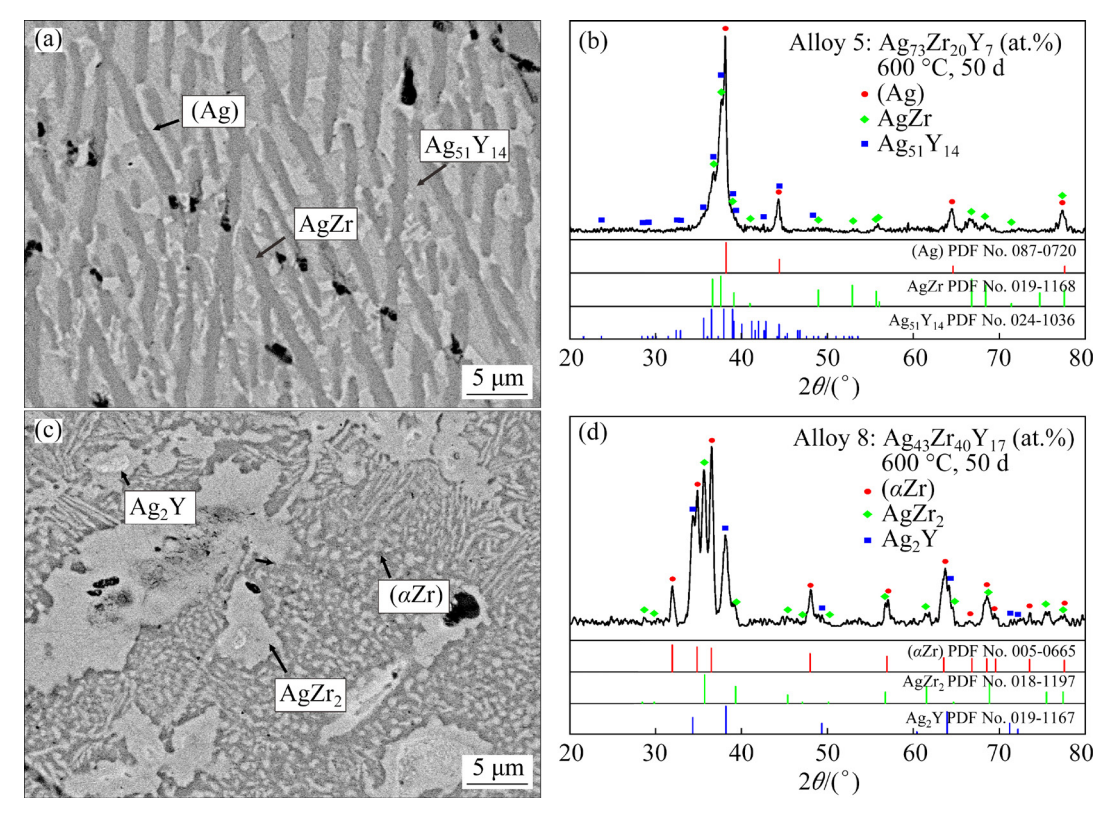


Fig. 4 BSE images (a, c) and XRD patterns (b, d) of Ag–Zr–Y alloys annealed at 600 °C for 50 d: (a, b) Alloy 5 (Ag₇₃Zr₂₀Y₇); (c, d) Alloy 8 (Ag₄₃Zr₄₀Y₁₇)

in low intensity and pretty hard distinguished in Fig. 4(b). Also combined with the composition by EDS and the region by BSE micrograph, the three-phase region of Alloy 5 was determined to consist of white (Ag) + dark AgZr + light gray Ag₅₁Y₁₄. Figures 4(c) and (d) show the BSE micrograph and XRD pattern for Alloy 8 (Ag₄₃Zr₄₀Y₁₇), respectively, which is located in the three-phase region, i.e., dark grey (αZr) + light grey $AgZr_2 + dark Ag_2Y$. Similarly, the phases of Alloys 6 (Ag₄₇Zr₂₀Y₃₃), 7 (Ag₅₄Zr₄₀Y₆) and 9 (Ag₁₄Zr₄₀Y₄₆) were also determined. Their XRD patterns are shown in Figs. 5(a), (b) and (c). Combined with the results of XRD pattern and EDS composition analysis, Alloys 6, 7 and 9 are located in threephase regions, i.e. $(\alpha Zr) + Ag_2Y + Ag_3Y + Ag_{51}Y_{14} +$ $AgZr + AgZr_2$ and $(\alpha Zr) + (\alpha Y) + AgY$, respectively. Based on the experimental analysis above, five three-phase regions (Ag) + AgZr + $Ag_{51}Y_{14}$, $AgZr + AgZr_2 + Ag_{51}Y_{14}$, $(\alpha Zr) + AgZr_2 +$ Ag_2Y , $(\alpha Zr) + Ag_2Y + AgY$ and $(\alpha Zr) + (\alpha Y) + AgY$ were determined at 600 °C. According to the phase regions of Alloys 7 and 8 and the Gibbs phase rule [36], a three-phase region $AgZr_2 + Ag_{51}Y_{14} + Ag_2Y$ was extrapolated. The measured solubilities of Ag and Zr in (α Y), Zr in $Ag_{51}Y_{14}$, Ag_2Y and AgY, and Y in $AgZr_2$ and AgZr are approximately 3.13, 9.73, 1.76, 1.90, 2.91, 0.50 and 1.25 at.%, respectively.

Alloys 10–12 were prepared to determine the isothermal section of the Ag–Zr–Y system annealed at 500 °C. Figure 6 shows the BSE micrographs and XRD patterns of representative Alloys 11 and 12, which were annealed at 500 °C for 60 d. In Alloy 11 (Ag₅₂Zr₁₀Y₃₈), the three-phase equilibrium dark AgY + light gray Ag₂Y + dark gray (α Zr) is observed in the BSE micrograph and confirmed by XRD pattern, as shown in Figs. 6(a) and (b). Likewise, Alloy 12 (Ag₆₀Zr₃₀Y₁₀) is located in the three-phase region, i.e., white Ag₅₁Y₁₄ + light gray AgZr + dark gray AgZr₂. The measured results are shown in Figs. 6(c) and (d). Similarly, the phase of

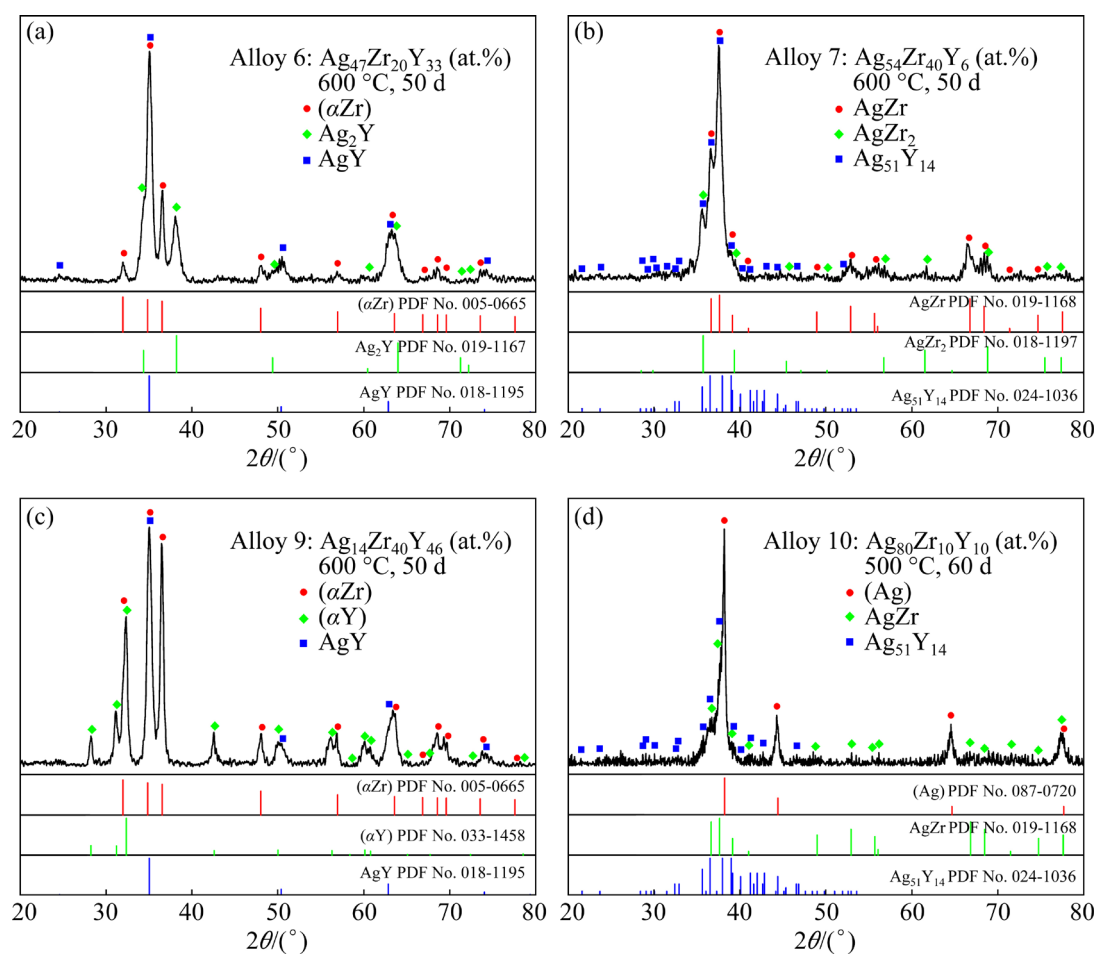


Fig. 5 XRD patterns of Ag–Zr–Y alloys: (a) Alloy 6 (Ag₄₇Zr₂₀Y₃₃); (b) Alloy 7 (Ag₅₄Zr₄₀Y₆); (c) Alloy 9 (Ag₁₄Zr₄₀Y₄₆); (d) Alloy 10 (Ag₈₀Zr₁₀Y₁₀)

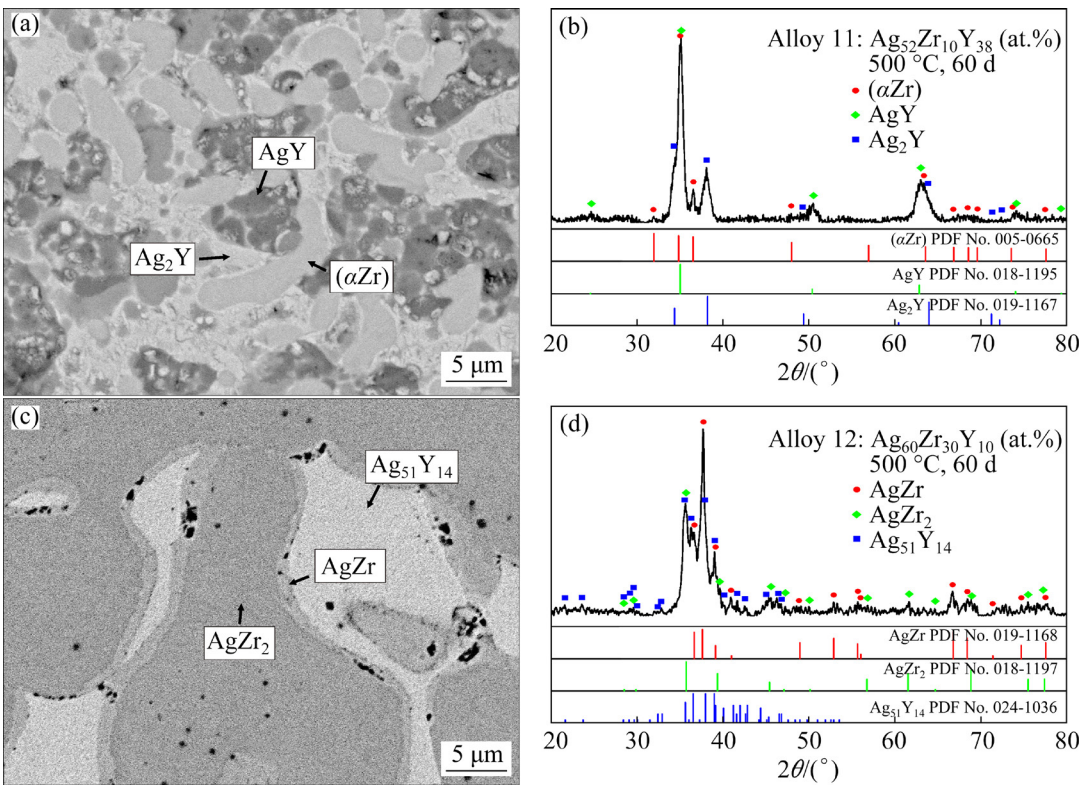


Fig. 6 BSE images (a, c) and XRD patterns (b, d) of Ag–Zr–Y alloys annealed at 500 °C for 60 d: (a, b) Alloy 11 $(Ag_{52}Zr_{10}Y_{38})$; (c, d) Alloy 12 $(Ag_{60}Zr_{30}Y_{10})$

Alloy 10 (Ag₈₀Zr₁₀Y₁₀) was also determined in the three-phase region, i.e., $(Ag) + AgZr + Ag_{51}Y_{14}$ by the results of XRD pattern and EDS composition analysis, as shown in the Fig. 5(d). Based on the experimental analysis above, the phase equilibria of the Ag-Zr-Y system annealed at 500 °C were obtained in the present work and three three-phase regions were determined as follows: (Ag) + AgZr + $Ag_{51}Y_{14}$, $AgZr + AgZr_2 + Ag_{51}Y_{14}$ and $(\alpha Zr) +$ Ag₂Y + AgY. According to the binary phase diagrams, the experimental data in the present work and the Gibbs phase rule [36], three three-phase regions $AgZr_2 + Ag_{51}Y_{14} + Ag_2Y$, $(\alpha Zr) + AgZr_2 +$ Ag₂Y and $(\alpha Zr) + (\alpha Y) + AgY$ were extrapolated. The phase equilibria of the Ag-Zr-Y system annealed at 600 and 500 °C are similar to those at 750 °C in the work of HE et al [14]. The measured solubilities of Zr in Ag₅₁Y₁₄, Ag₂Y and AgY and Y in AgZr₂ and AgZr are about 0.95, 1.02, 2.35, 0.02 and 1.06 at.% at 500 °C, respectively.

It is worth noting that some phases shown in Fig. 2(a) and Fig. 6(a) are fine. It may be AgY precipitated on coarse phases. In order to reduce the influences of fine precipitates, when performing EDS measurements, the center of the relatively

large phase region was selected. By comparing the measured results of large and small phase fields, it was found that both results are close. This means that the compositions measured by EDS are very little affected by the surrounding phases or fine precipitates. As AgZr₂ phase has the highest melting point of compounds in the Ag-Zr-Y system, homogeneously annealing at 600 and 500 °C is difficult to eliminate the as-cast structure in samples, as can be seen in Figs. 4(c) and 6(c). Even so, comparing the EDS composition analysis in the present work with the results by EPMA at 750 °C annealing for 90 d of HE et al [14], the composition of each phase is homogeneous and there is no macro or dendrite segregation. Thus, the samples are basically in the equilibrium state and the experimental results are acceptable.

Based on the experimental results, the solubilities of the third element in $Ag_{51}Y_{14}$, Ag_2Y , $AgZr_2$ and AgZr decrease with the decrease of temperature except AgY. In the present work, near the Ag–Zr side, the average measured solubilities of Y in (αZr) are very small and negligible and those of Ag in (αZr) at 800, 600 and 500 °C are about 2.12, 4.45 and 3.22 at.%, respectively. The

solubilities of Y and Zr in (Ag) at 600 and 500 °C are approximately 1.89, 4.49, 1.00 and 0.69 at.%, respectively. Due to close packing of hcp and fcc structures, the solubilities of solution phases should not be large in the Ag–Zr–Y system. Considering this reason, the solubility of Ag in the (Zr) phase at 600 °C and that of Y in the (Ag) phase at 500 °C are slightly large maybe due to the experimental error. The measured solubilities of the third element in Ag₅₁Y₁₄ and AgZr₂ are smaller and those in Ag₂Y, AgY and AgZr are larger than the corresponding values at 750 °C from HE et al [14]. All the experimental results were accepted to use for the analysis of the phase equilibria and optimization of the Ag–Zr–Y system.

5.2 Thermodynamic calculation results and discussion

Based on the experimental data available in the present work and the literature [14], the Ag–Zr–Y system was evaluated by the optimization module PARROT [37] of Thermo-Calc software, which works by minimizing the square sum of the differences between the experimental results and calculated values. First, the solubilities of the third element in binary phases were optimized. Then, the data of three-phase region in the isothermal sections at 800, 750, 600 and 500 °C were considered one by one. Finally, all parameters were optimized simultaneously to achieve a set of self-consistent thermodynamic parameters of the Ag–Zr–Y system, which were listed in Table 3.

The calculated isothermal sections of the Ag–Zr–Y system at 800, 750, 600 and 500 °C are shown in Fig. 7. Seven three-phase regions in the isothermal section at 800 °C were calculated and shown in Fig. 7(a). The calculated solubilities of the other element in (αY) and (αZr) are all very small and negligible. The calculated solubilities of Zr in Ag₅₁Y₁₄, Ag₂Y and AgY and Y in AgZr₂ are 2.33, 2.60, 2.83 and 1.01 at.%, respectively, which are consistent with the experimental results of 2.10, 2.35, 2.22 and 0.89 at.%, respectively. The calculated isothermal section at 800 °C is in good agreement with the measured ones.

The calculated isothermal section at 750 °C has six three-phase regions in Fig. 7(b). The calculated phase equilibria are consistent with the measured ones by HE et al [14]. The calculated solubilities of the other two elements in (αY) , (αZr) and (Ag) are also very small. The calculated solubilities of Zr in Ag₅₁Y₁₄ and Y in AgZr₂ are 2.22 and 0.82 at.%, respectively, which are consistent with the measured ones by HE et al [14]. However, the calculated solubilities of Zr in Ag₂Y and AgY and Y in AgZr are 2.34, 2.64 and 1.65 at.%, respectively, which are larger than those measured by HE et al [14]. This is because the solubilities of these phases at 800, 600 and 500 °C measured by the present work are larger than those measured at 750 °C by HE et al [14]. During the optimization process, the experimental solubility data by the present work were given with larger weights than the data from HE et al [14].

Table 3 Thermodynamic parameters of Ag-Zr- Y system in present work

Phase	Model	Thermodynamic parameter
Liquid	$(Ag,Y,Zr)_1$	$^{0}L_{\mathrm{Ag, Y, Zr}}^{\mathrm{liquid}} = 25000$
AgZr	$(Ag)_1(Y,Zr)_1$	${}^{o}G_{Ag;Y}^{AgZr} = -59989 + 8.815T + {}^{o}G_{Ag}^{fcc} + {}^{o}G_{Y}^{hcp}$
$AgZr_2$	$(Ag)_1(Y,Zr)_2$	${}^{o}G_{Ag:Y}^{AgZr_2} = -59989 + 22.356T + {}^{o}G_{Ag}^{fcc} + 2{}^{o}G_{Y}^{hcp}$
AgY	$(Ag)_1(Y,Zr)_1$	${}^{o}G_{Ag:Zr}^{AgY} = -11898 + 10.994T + {}^{o}G_{Ag}^{fcc} + {}^{o}G_{Zr}^{hcp}$
Ag_2Y	$(Ag)_2(Y,Zr)_1$	${}^{o}G_{Ag:Zr}^{Ag_2Y} = -10999 + 5.262T + 2{}^{o}G_{Ag}^{fcc} + {}^{o}G_{Zr}^{hcp}$
	$(Ag)_{51}(Y,Zr)_{14}$	${}^{o}G_{Ag;Y}^{Ag_{51}Y_{14}} = -1493765 + 50.310T + 51{}^{o}G_{Ag}^{fcc} + 14{}^{o}G_{Y}^{hcp}$
$Ag_{51}Y_{14}$		${}^{o}G_{Ag;Zr}^{Ag_{51}Y_{14}} = 20093+59.150T + 51{}^{o}G_{Ag}^{fcc} + 14{}^{o}G_{Zr}^{hcp}$

Temperature (*T*) was in K and Gibbs energy was in J/mol. The Gibbs energies for the pure elements were taken from SGTE database compiled by DINSDALE [30]. The thermodynamic parameters for the Ag–Zr, Ag–Y and Zr–Y systems from HSIAO et al [18], WANG et al [26] and BU et al [29], respectively, were adopted in the present work.

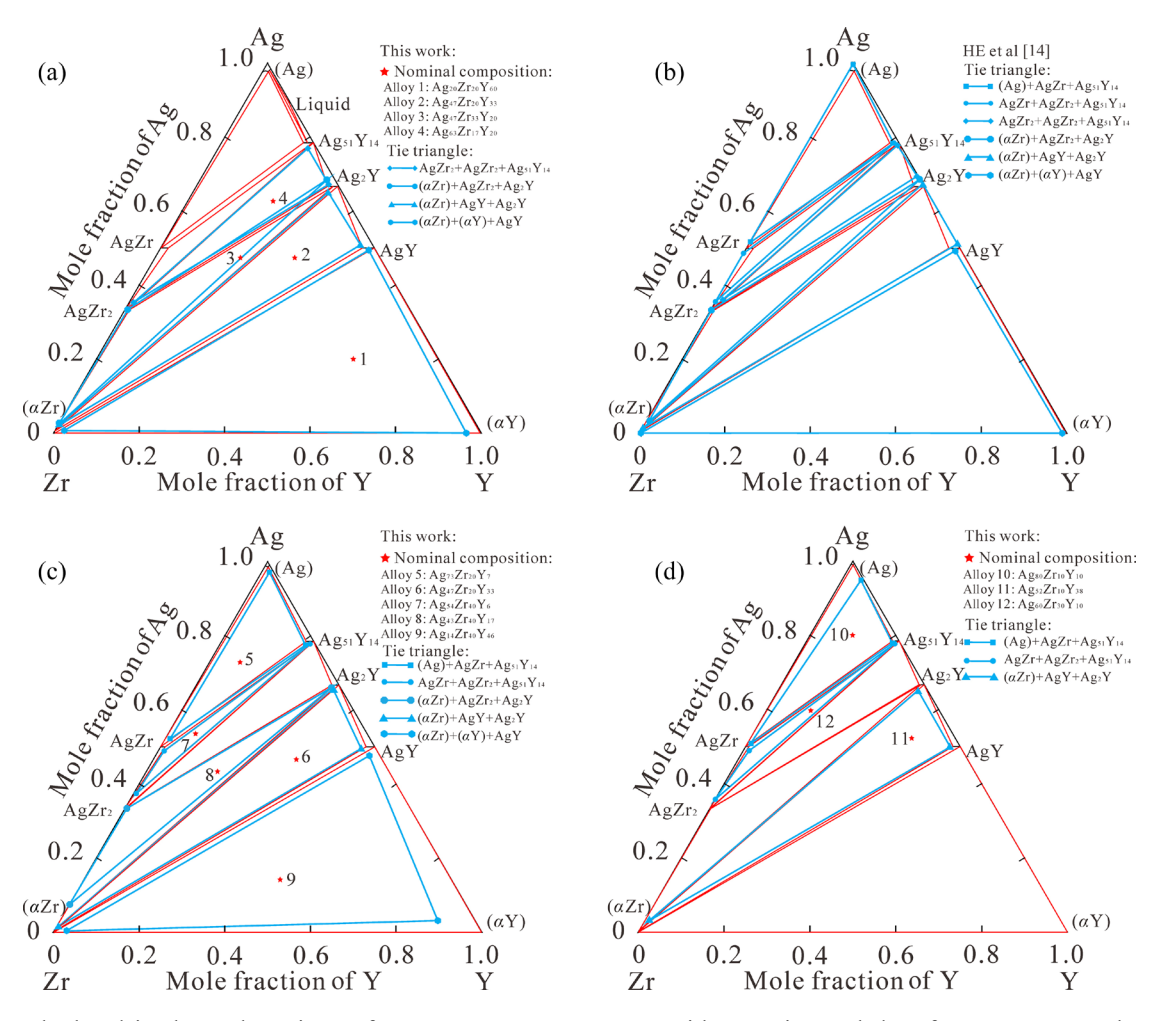


Fig. 7 Calculated isothermal sections of Ag–Zr–Y ternary system with experimental data from present work and HE et al [14]: (a) 800 °C; (b) 750 °C; (c) 600 °C; (d) 500 °C

Six three-phase regions in the isothermal sections at 600 and 500 °C were calculated and shown in Figs. 7(c) and (d), respectively. The calculated isothermal sections at 600 and 500 °C are similar to those at 750 °C. The calculated solubilities of Zr in Ag₅₁Y₁₄, Ag₂Y, AgY and Y in AgZr₂ and AgZr are 1.81, 1.66, 2.06, 0.40 and 1.10 at.% at 600 °C, respectively, and 1.49, 1.22, 1.65, 0.21 and 0.79 at.% at 500 °C, respectively, which are consistent with the present experimental results. The calculated solubilities of the other two elements in the (αY) , (αZr) and (Ag) at 600 and 500 °C are negligible. The calculated isothermal sections at 600 and 500 °C are in good agreement with the measured ones except for two data points in the Y-rich corner at 600 °C and the Ag-rich corner at 500 °C. According to the low solubilities of Ag and Zr in the (αY) phase and those of Y in the (Ag) phase in the Ag-Y [26] and Zr-Y [29] binary systems below 600 °C, ternary interaction parameters of the other two elements in the (αY) and (Ag) phases have almost no influence on the solubilities of the other two elements in the (αY) and (Ag) phases. Considering the experimental results of these regions at 800 and 750 °C, the two experimental points at 600 and 500 °C were not used during optimization. Thus, the calculated solubilities of the other two elements in the (αY) and (Ag) phases are slightly less than the experimental values.

The liquidus projection and reaction scheme have been proved to be a useful tool in describing ternary and higher order systems. The liquidus projection of the Ag–Zr–Y system was calculated by Pandat software [38,39], as shown in Fig. 8. The constructed reaction scheme is shown in Fig. 9. The calculated invariant reactions are listed in Table 4. Fifteen invariant reactions were predicted.

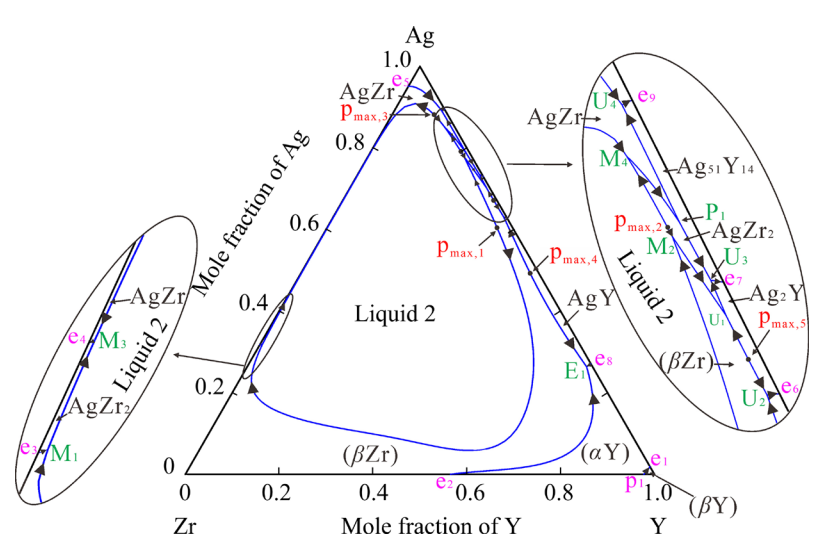


Fig. 8 Calculated liquidus projection of Ag-Zr-Y system

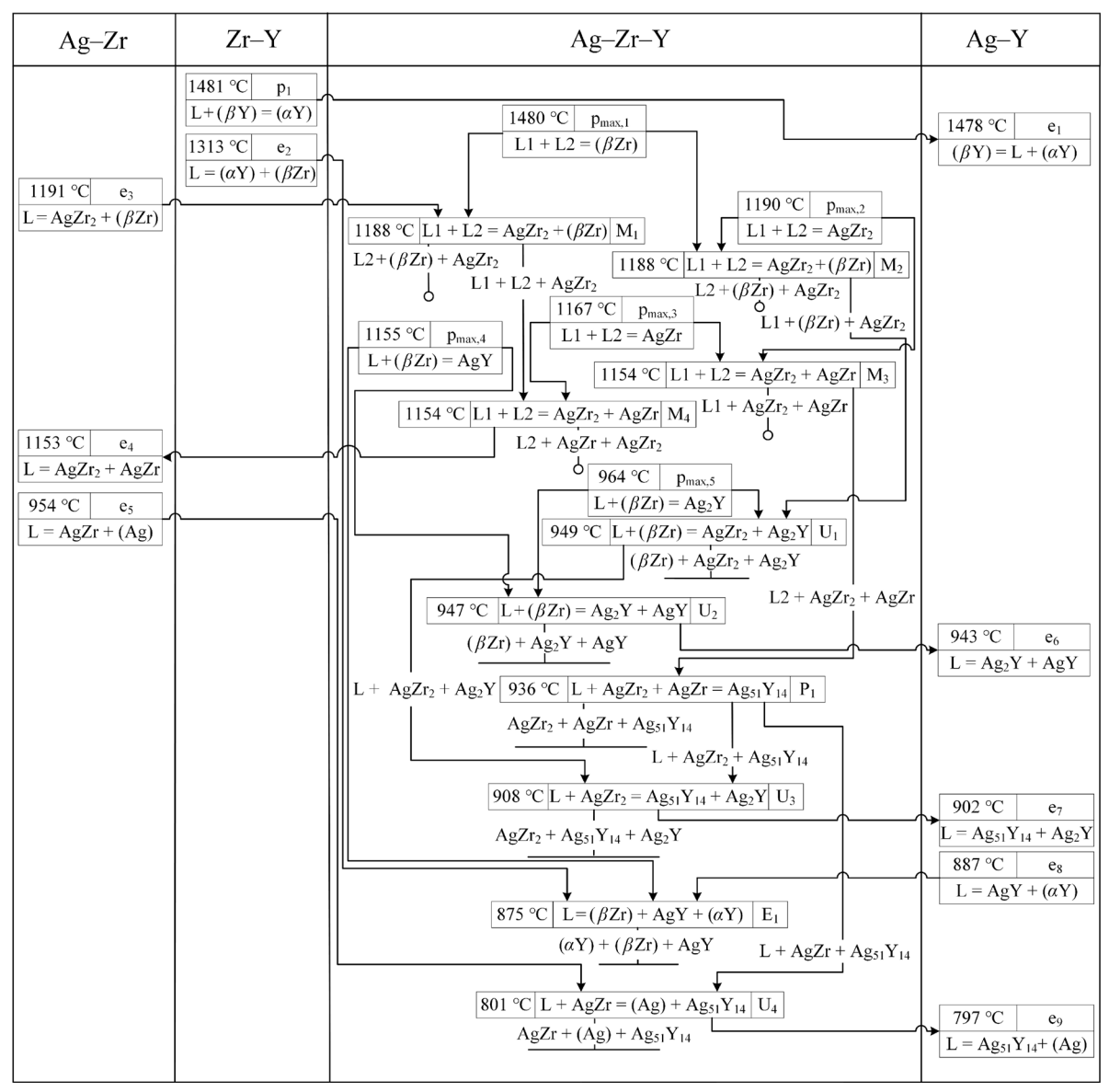


Fig. 9 Constructed reaction scheme of Ag-Zr-Y system (L, L1 and L2 represent Liquid, Liquid 1 and Liquid 2, respectively)

Table 4 Calculated invariant reactions in Ag–Zr–Y system

Туре	Invariant reaction	Tomor oroture /ºC	Composition/at.%		
	invariant reaction	Temperature/°C	Ag	Zr	Y
M_1	Liquid 1 + Liquid 2 = $AgZr_2 + (\beta Zr)$	1188	31.85	67.68	0.47
M_2	Liquid 1 + Liquid 2 = $AgZr_2 + (\beta Zr)$	1188	77.83	1.63	20.54
M_3	Liquid 1 = Liquid 2 + $AgZr_2 + AgZr$	1154	84.95	2.14	12.91
M_4	Liquid 1 + Liquid 2 = $AgZr_2 + AgZr$	1154	31.69	67.77	0.54
P ₁	$Liquid + AgZr_2 + AgZr = Ag_{51}Y_{14}$	936	78.71	0.75	20.54
U_1	$Liquid + (\beta Zr) = AgZr_2 + Ag_2Y$	949	70.30	0.68	29.02
U_2	$Liquid + (\beta Zr) = Ag_2Y + AgY$	947	63.06	0.59	36.35
U_3	$Liquid + AgZr_2 = Ag_{51}Y_{14} + Ag_2Y$	908	73.45	0.57	25.98
U_4	$Liquid + AgZr = (Ag) + Ag_{51}Y_{14}$	801	89.27	0.79	9.94
E ₁	$Liquid = (\beta Zr) + AgY + (\alpha Y)$	875	26.38	1.27	72.35
p _{max,1}	Liquid 1 + (βZr) = Liquid 2	1480	60.43	3.32	36.25
$p_{\text{max},2}$	Liquid $1 + \text{Liquid } 2 = \text{AgZr}_2$	1190	79.11	1.69	19.20
$p_{\text{max},3}$	Liquid $1 + \text{Liquid } 2 = \text{AgZr}$	1167	88.13	2.89	8.98
$p_{\text{max,4}}$	$Liquid + (\beta Zr) = AgY$	1155	49.17	1.85	48.98
p _{max,5}	$Liquid + (\beta Zr) = Ag_2Y$	964	67.22	0.66	32.12

With the help of key experiments and CALPHAD method, a set of self-consistent thermodynamic parameters of the Ag–Zr–Y system were obtained, which enriched the thermodynamic database of the Ag-based multicomponent alloys. By using the thermodynamic database, the phase equilibria and thermodynamic properties of the Ag-based multicomponent alloys can be predicted for helping design and manufacture of the new alloys.

6 Conclusions

- (1) By means of XRD and SEM-EDS methods, the phase equilibria of the Ag-Zr-Y system at 800, 600, and 500 °C were investigated. No ternary compound was found in these isothermal sections. Seven three-phase regions at 800 °C and six three-phase regions at 600 and 500 °C were determined or extrapolated.
- (2) At 600 °C the measured solubilities of Y in (αZr) are very small and negligible, and those of Ag in (αZr) , Y and Zr in (Ag) and Ag and Zr in (αY) are about than 4.45, 1.89, 1.00, 3.13 and 9.73, respectively. The measured solubilities of Zr in Ag₅₁Y₁₄ and Ag₂Y and Y in AgZr₂ decrease with the decrease of temperature and those at 800 °C are about 2.10, 2.35 and 0.89 at.%, respectively. Those

of Zr in AgY at 800, 600 and 500 °C are about 2.22, 2.91 and 2.35 at.%, respectively.

(3) Based on the experimental phase equilibria data, the Ag–Zr–Y system was assessed by means of the CALPHAD method. A set of self-consistent thermodynamic parameters were obtained. The isothermal sections at 800, 750, 600 and 500 °C and liquidus projection were calculated. The reaction scheme for the Ag–Zr–Y system was constructed. Most of the reliable experimental results can be well reproduced by the present thermodynamic modeling.

Acknowledgments

The authors are grateful for the financial supports from the National Natural Science Foundation of China (No. 52071002), the Major Science and Technology Project of Precious Metal Materials Genetic Engineering in Yunnan Province, China (No. 202002AB080001-1), and the National Natural Science Foundation of Anhui Province, China (No. 2008085QE200).

References

[1] MATURI M, LOCATELLI E, SAMBRI L, TORTORELLA S, ŠTURM S, KOSTEVŠEK N, COMES FRANCHINI M. Synthesis of ultrasmall single-crystal gold–silver alloy

- nanotriangles and their application in photothermal therapy [J]. Nanomaterials, 2021, 11(4): 912.
- [2] REDDY K L, KUMAR S, KUMAR A, KRISHNAN V. Wide spectrum photocatalytic activity in lanthanide-doped upconversion nanophosphors coated with porous TiO₂ and Ag-Cu bimetallic nanoparticles [J]. Journal of Hazardous Materials, 2019, 367: 694-705.
- [3] ZHAO Di, FU Li, LIU Hong-yan, CHEN Yu, LI Gui-hua, ZHANG Xin-yi, DU Yun-zhi, MA Jia-rou. Charge transfer mechanism and photoelectrocatalytic activity of Ag@AgBr/ GO/Ni plasma photocathode film electrode [J]. The Chinese Journal of Nonferrous Metals, 2021, 31(12): 3614–3623. (in Chinese)
- [4] PIRHAYATI P, JAMSHIDI AVAL H. Microstructural characterization and mechanical properties of friction surfaced AA2024–Ag composites [J]. Transactions of Nonferrous Metals Society of China, 2020, 30(7): 1756–1770.
- [5] CHEN Hao, ZHOU Long-hai, XUE Jing-jing, ZHAO Tao. Study on the microstructure of Ag-Y alloy [J]. Precious Metals, 2019, 40(3): 6–10. (in Chinese)
- [6] ZHANG Dong-dong, LIU Chu-ming, JIANG Shu-nong, WAN Ying-chun, CHEN Zhi-yong. Effects of trace Ag on precipitation behavior and mechanical properties of extruded Mg-Gd-Y-Zr alloys [J]. Transactions of Nonferrous Metals Society of China, 2021, 31(11): 3394–3404.
- [7] LIU Wei, WU Bo-qiang, LIU Hai-rong, LIU Rang-su, MO Yun-fei, TIAN Ze-an, HOU Zhao-yang, XI Ting-fei, WAN Zhi-yi, HUANG Chang-xiong, CHEN Xin. Simulation on microstructure evolution and mechanical properties of Mg-Y alloys: Effect of trace Y [J]. Transactions of Nonferrous Metals Society of China, 2022, 32(3): 812–823.
- [8] SONG Wen-jie, DONG Hui-ping, LIU Jie, ZHANG Guang, LIU Yan-hui. Effect of Y on microstructure and mechanical properties of as-cast Mg-8Li-3Al-3Zn alloy [J]. The Chinese Journal of Nonferrous Metals, 2021, 31(1): 1–8. (in Chinese)
- [9] CHANG Li-li, GUO Jing, SU Xiao-jing. Effect of Y on microstructure evolution and mechanical properties of Mg-4Li-3Al alloys [J]. Transactions of Nonferrous Metals Society of China, 2021, 31(12): 3691-3702.
- [10] LI Qing-lin, LI Bin-qiang, LI Jin-bao, ZHU Yu-qian, XIA Tian-dong. Effect of yttrium addition on the microstructures and mechanical properties of hypereutectic Al–20Si alloy [J]. Materials Science and Engineering: A, 2018, 722: 47–57.
- [11] LI Dong-qing, ZHOU Li-xian, ZHANG Jun, WANG Jing-chao, GU Jian, SI Jia-jun. Enhanced alumina film adhesion of Hf/Y-doped iron-aluminum alloys during high-temperature oxidation: A new observation [J]. Rare Metals, 2019, 38(9): 877–884.
- [12] XIANG Xiong-zhi, BAI Xiao-jun, CHEN Peng-xu. Anti-tarnish property of sterling silver alloy with yttrium addition [J]. Rare Metals, 2012, 31(5): 438–441.
- [13] GAGANOV A, FREUDENBERGER J, BOTCHAROVA E, SCHULTZ L. Effect of Zr additions on the microstructure, and the mechanical and electrical properties of Cu-7 wt.%Ag alloys [J]. Materials Science and Engineering: A, 2006, 437(2): 313–322.
- [14] HE X C, WANG Y M, LIU H S, JIN Z P. Investigation of

- the isothermal section of the Ag–Zr–Y ternary system at 1023 K by diffusion-triple [J]. Journal of Alloys and Compounds, 2006, 417(1/2): L1–L3.
- [15] HU Biao, ZHANG Hua-qing, ZHANG Jin, YANG Ming-jun, DU Yong, ZHAO Dong-dong. Progress in interfacial thermodynamics and grain boundary complexion diagram [J]. Acta Metallurgica Sinica, 2021, 57(9): 1199–1214. (in Chinese)
- [16] ZHANG Yu, HU Biao, ZENG Gang, LIU Shu-hong, DU Yong, YIN Hui-qin. Experimental investigation, thermodynamic modeling and solidified microstructure of the Cu-Ti-Nb ternary system [J]. Calphad, 2022, 76: 102395.
- [17] QIAO Hui, ZHANG Yu, HU Biao, LI Kai, LIU Shu-hong, DU Yong. Experimental investigation of the phase equilibria in the Ti–Al–Mo–V–Cr key quaternary systems at 700 and 800 °C [J]. The Chinese Journal of Nonferrous Metals, 2022, 32(9): 2620–2632. (in Chinese)
- [18] HSIAO H M, LIANG Song-mao, SCHMID-FETZER R, YEN Y W. Thermodynamic assessment of the Ag–Zr and Cu–Zr binary systems [J]. Calphad, 2016, 55: 77–87.
- [19] GSCHNEIDNER K A, CALDERWOOD F W. The Ag-Y (silver-yttrium) system [J]. Bulletin of Alloy Phase Diagrams, 1983, 4(4): 377–379.
- [20] ZHANG Kang-hou, ZHAO Huai-zhi, ZHOU Yue-hua. An investigation of the Ag-Zr phase diagram [J]. Journal of the Less Common Metals, 1988, 138(2): 173-177.
- [21] FITZNER K, KLEPPA O J. Thermochemistry of binary alloys of transition metals: The Me-Ti, Me-Zr, and Me-Hf (Me=Ag, Au) systems [J]. Metallurgical Transactions A, 1992, 23(3): 997–1003.
- [22] KARAKAYA I, THOMPSON W T. The Ag–Zr (silver–zirconium) system [J]. Journal of Phase Equilibria, 1992, 13(2): 143–146.
- [23] HE X C, WANG H, LIU H S, JIN Z P. Thermodynamic description of the Cu-Ag-Zr system [J]. Calphad, 2006, 30(4): 367-374.
- [24] KANG D H, JUNG I H. Critical thermodynamic evaluation and optimization of the Ag–Zr, Cu–Zr and Ag–Cu–Zr systems and its applications to amorphous Cu–Zr–Ag alloys [J]. Intermetallics, 2010, 18(5): 815–833.
- [25] MCMASTERS O D, GSCHNEIDER K A, VENTEICHER R F. Crystallography of the silver-rich rare-earth-silver intermetallic compounds [J]. Acta Crystallographica B, 1970, 26(9): 1224–1229.
- [26] WANG S L, WANG C P, LIU X J, ISHIDA K. Thermodynamic assessments of the Ag-Y and Sc-Y systems [J]. Journal of Alloys and Compounds, 2009, 476(1/2): 187–192.
- [27] WANG Jian, ZHANG Zhang, JUNG I H, RAO Wei-feng. Critical evaluation and thermodynamic modeling of the Ag–X (X=Mn, Y, Sr) binary systems [J]. Intermetallics, 2021, 136: 107260.
- [28] PALENZONA A, CIRAFICI S. The Y–Zr (yttrium–zirconium) system [J]. Journal of Phase Equilibria, 1991, 12(4): 485–489.
- [29] BU M J, WANG P S, XU H H, LIU S H, SHA C S, DU Y, PAN F S, TANG A T. Experimental investigation and thermodynamic modeling of the Zr-Y system [J]. Journal of Mining and Metallurgy, 2010, 46(2): 181–192.

- [30] DINSDALE A T. SGTE data for pure elements [J]. Calphad, 1991, 15(4): 317–425.
- [31] SHI Hui, LI Qian, ZHANG Jie-yu, LUO Qun, CHOU K C. Re-assessment of the Mg-Zn-Ce system focusing on the phase equilibria in Mg-rich corner [J]. Calphad, 2020, 68: 101742.
- [32] LUO Qun, ZHAI Cong, GU Qin-fen, ZHU Wen-fei, LI Qian. Experimental study and thermodynamic evaluation of Mg-La-Zn system [J]. Journal of Alloys and Compounds, 2020, 814: 152297.
- [33] REDLICH O, KISTER A T. Algebraic representation of thermodynamic properties and the classification of solutions
 [J]. Industrial & Engineering Chemistry, 1948, 40(2): 345–348.
- [34] HILLERT M, STAFFANSSON L I. The regular-solution model for stoichiometric phases and ionic melts [J]. Acta Chemica Scandinavica, 1970, 24(10): 3618–3626.

- [35] SUNDMAN B, ÅGREN J. A regular solution model for phases with several components and sublattices, suitable for computer applications [J]. Journal of Physics and Chemistry of Solids, 1981, 42(4): 297–301.
- [36] LUO Qun, ZHAI Cong, SUN Dong-ke, CHEN Wei, LI Qian. Interpolation and extrapolation with the CALPHAD method [J]. Journal of Materials Science & Technology, 2019, 35(9): 2115–2120.
- [37] SUNDMAN B, JANSSON B, ANDERSSON J. The thermocalc databank system [J]. Calphad, 1985, 9(2): 153–190.
- [38] CHEN Shuang-lin, CAO Wei-sheng, ZHANG Chuan, ZHU Jun, ZHANG Fan, LI Qian, ZHANG Jie-yu. Calculation of property contour diagrams [J]. Calphad, 2016, 55: 63–68.
- [39] LUO Qun, CHEN Shuang-lin, ZHANG Jie-yu, LI Lin, CHOU K C, LI Qian. Experimental investigation and thermodynamic assessment of Nd-H and Nd-Ni-H systems [J]. Calphad, 2015, 51: 282–291.

Ag-Zr-Y 体系相平衡的实验测定与热力学计算

金程刚 1,2, 胡 标 1,2, 石愈超 1,2, 盛绍顶 1,2, 刘树红 3, 杜 勇 3, 胡洁琼 4

- 1. 安徽理工大学 材料科学与工程学院,淮南 232001;
- 2. 安徽理工大学 安徽省纳米碳基材料与环境健康国际联合研究中心,淮南 232001;
 - 3. 中南大学 粉末冶金国家重点实验室,长沙 410083;
 - 4. 中国贵金属控股有限公司, 昆明 650000

摘 要:利用 XRD、SEM-EDS 技术研究 Ag-Zr-Y 体系在 800、600 和 500 $^{\circ}$ 的相平衡。测定 Y 在 Ag2Zr 和 AgZr 相以及 Zr 在 Ag51Y14、Ag2Y 和 AgY 相中的溶解度。在这些相图的等温截面中未发现三元化合物的存在。根据本研究和文献报道的实验数据,采用 CALPHAD 相图计算方法对 Ag-Zr-Y 体系进行热力学评估。采用置换溶液模型描述熔体相以及亚点阵模型描述二元化合物。通过优化得到一套自治且能准确描述 Ag-Zr-Y 体系的热力学参数。计算几个代表性的等温截面和液相面投影图,并构筑 Ag-Zr-Y 体系的希尔反应图。计算结果与实验数据相吻合。

关键词: Ag-Zr-Y 三元体系; 相平衡; 实验测定; 热力学模型; CALPHAD 方法

(Edited by Wei-ping CHEN)